 doi:10.20944/preprints202102.0303.v1

Article

Peculiarities of micro-mechanical behavior of 3D-printed aluminium alloy: *in situ* SEM study

Eugene S. Statnik [1], Kirill V. Nyaza [2], Alexey I. Salimon[1,*], Dmitry Ryabov[2], and Alexander M. Korsunsky [1,3]

[1] HSM lab, Center for Energy Science and Technology, Skoltech, Moscow 121205, Russia; eugene.statnik@skoltech.ru; a.korsunsky@skoltech.ru
[2] Light Materials and Technologies Institute, UC RUSAL, Moscow 121096, Russia; mobiad@yandex.ru, dmitriy.ryabov2@rusal.com
[3] MBLEM, Department of Engineering Science, University of Oxford, Oxford OX1 3PJ, United Kingdom
* Correspondence: a.salimon@skoltech.ru

Abstract: 3D-printed aluminium alloy fabrications made by selective laser melting (SLM) offer a promising route for the production of small series of custom-designed heat exchangers with complex geometry and shape and miniature size. Alloy composition and printing parameters need to be optimized to mitigate fabrication defects (pores and microcracks) and enhance the part performance. The deformation response needs to be studied with adequate characterization techniques at relevant dimensional scale capturing the peculiarities of micro-mechanical behavior relevant to the particular article and specimen dimensions. Purposefully designed Al-Si-Mg 3D-printable RS-333 alloy was investigated with a number of microscopy techniques including *in situ* mechanical testing with a Deben Microtest 1 kN stage integrated and synchronized with Tescan Vega3 SEM to acquire high resolution image datasets for Digital Image Correlation (DIC) analysis. Dog bone specimens were 3D-printed in different orientation of gauge zone cross-section with respect to the fast laser beam scanning and growth directions. This corresponds to varying local conditions of metal solidification and cooling. Specimens show variation in mechanical properties, namely, Young's modulus (65…78 GPa), yield stress (80–150 MPa), ultimate tensile strength (115–225 MPa) and elongation at break (0,75–1,4 %). Furthermore, the failure localization and character was altered with the change of gauge cross-section orientation. DIC analysis allowed correct strain evaluation that overcame the load frame compliance effect and helped to identify the unevenness of deformation distribution (plasticity waves) that ultimately resulted in exceptionally high strain localization near the ultimate failure crack position.

Keywords: RS-333 alloy, SLM 3DP, *in situ* SEM tensile testing, DIC analysis, *Ncorr*

1. Introduction

Having seen rapid development since early 2000s, the additive CAD/CAM technology of selective laser melting (SLM) 3D printing of metal alloys has expanded towards aluminium alloys in 2010s [1-3]. Important aspects such as alloy composition, laser scanning rate and post-processing parameters were systematically investigated to reach eventually desirable mechanical performance [4-6]. Rooted from widely-used near-eutectic casting Al-Si alloys, printable Al-Si-Mg alloys facilitate the formation of parts with low porosity due to the prolonged solidification and good flowability leading to superior casting behavior and low susceptibility to hot-cracking. The moderation of liquid phase viscosity by means of doping Al-Zn-Mg-Cu high strength alloys with secondary alloying elements (Zr, Mn, Fe, Co and others) reduces the probability of undesired defect assemblies (pores and coarse dendrite grains) down to acceptable level [4]. Moreover, transition elements such as Zr, Ti or Mn have strong grain refining effect leading to significant improvement in the resistance to hot cracking due to decreased size of dendrites that allow better liquid metal support of solid-liquid regions during solidification. Introduction of such elements even in the form of nano-sized particles is considered to be an efficient

Preprints (www.preprints.org) | NOT PEER-REVIEWED | Posted: 12 February 2021 doi:10.20944/preprints202102.0303.v1

means of improving printability [7]. Nevertheless, other phenomena must be taken into consideration that occur at hierarchically different dimensional structural levels. This include metallurgical aspects (formation of oxide inclusions, liquation and inherited component inhomogeneity) and thermo-mechanical processes (cracking and residual stresses caused by strong thermal gradients and solidification shrinkage). Control over these phenomena is required in order to optimize the mechanical and functional performance of 3D-printable aluminum alloys and components to attain high geometric fidelity of 3D-printed parts [8].

Technologically, the more complex printable aluminum alloys present a number of advantages in comparison with their traditional counterparts for niche applications where longer production time per article is tolerable. Prototypes, single units or small batches of miniature parts having complex geometry for use in fine mechanics applications, computer components and gadget hardware and robotics currently represent an obvious scope for SLM technology evolution [9].

Additive manufacturing technologies can find application when specific combinations of properties are sought such as for miniature heat exchangers of least mass or volume when both high strength and thermal conductivity are required. The performance indices to be minimized according to Ashby [10] are $\frac{\rho}{\sigma_y^2 \cdot \lambda}$ and $\frac{1}{\sigma_y^2 \cdot \lambda}$ respectively, where ρ is density, σ_y is yield strength and λ is the thermal conductivity.

Traditionally, heat exchangers are fabricated of 1XXX, 3XXX (Al-Mn) or 6XXX (Al-Mg-Si) series alloys. On the other hand, new aluminum alloys purposefully optimized for 3D printing possess both higher strength (compared to traditional AlSi10Mg alloy used in 3D printing) and improved thermal properties. Though aluminum-based materials should have in general high thermal conductivity [11] favorable to produce various parts for heat exchangers, 3D-printable AlSi10Mg alloy manifests moderate heat conductivity. 6XXX alloys do possess rather high strength and acceptable thermal conductivity as shown in Figure 1, but alloys such as 6061 are prone to cracking during the printing process [12], prompting to seek new alloy formulations to adopt for AM processes. Composition of 3D-printable RS-333 alloy from Al-Mg-Si system (which is considered in this paper) was tuned by design to improve castability and thereby to substitute 6061 aluminium alloy in heat exchange applications.

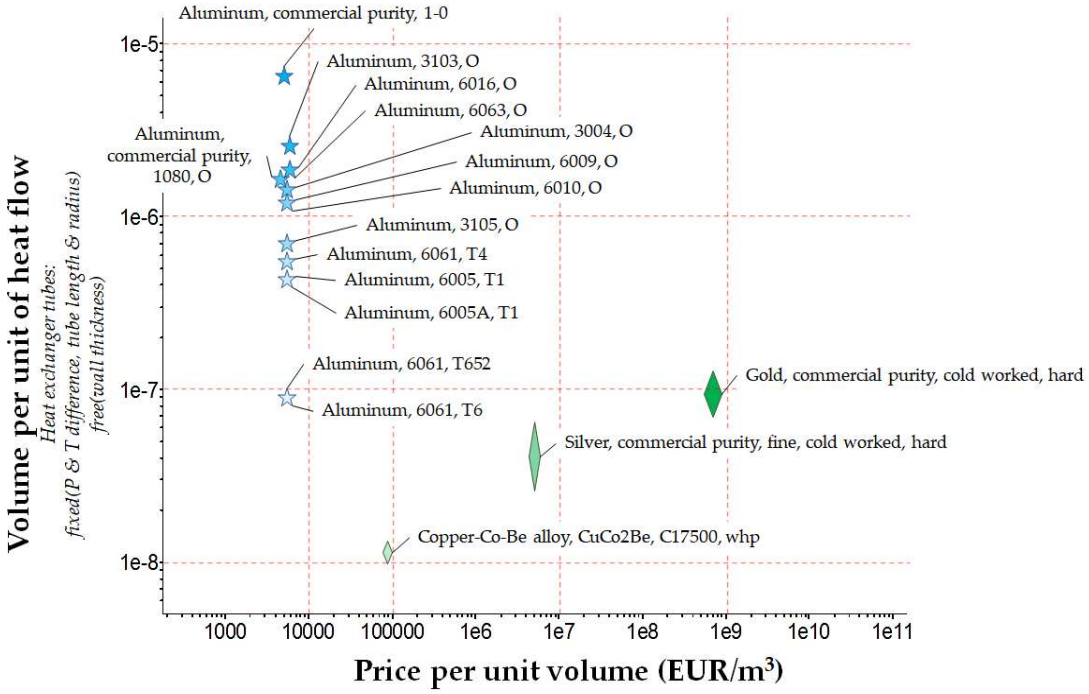

Figure 1. Comparison of some materials used in heat exchanging applications [13].

Preprints (www.preprints.org) | NOT PEER-REVIEWED | Posted: 12 February 2021 doi:10.20944/preprints202102.0303.v1

Mechanical microscopy methods that couple optical and/or electron microscopy with mechanical testing and advanced digital image analysis have been rapidly developing in recent decades [14-18]. These methods are particularly suitable for *in situ* mechanical testing of near-net-shape miniature and thin parts inside SEM chamber, since the deformation and fracture behavior can be visualized and studied at high resolution readily applicable to digital image correlation (DIC) analysis to reveal the peculiarities of deformation at the micrometer scale. Moreover, SLM 3D-printing of miniature fine mechanics parts having slim cross-sections puts forward cooling and solidification conditions different from those characteristics for conventional engineering articles.

We report our findings in a systematic study of the micro-mechanical behavior of tensile samples made from 3D-printable alloy RS-333. The acquisition of high-resolution SEM images was synchronized during *in situ* in-SEM tensile testing of dog bone samples 3D-printed in different relative orientation of the laser scanning and growth directions. DIC analysis is used to map the strain distribution and thus to trace the localization of strains in the vicinity of the major crack. The interpretation of the experimental findings suggests a correlation between the duration of the effective cooling period for elementary added material volumes, on the one hand, and the mechanical performance on the other.

2. Materials and Methods

The powder of RS-333 (AlSi3Mg0.5) alloy was supplied by "Valcom-PM" Ltd. (Volgograd, Russia). The powder was produced by nitrogen atomization method. Particle size varied over the range 20…63 μm with D50 = 42 μm according to the data from laser particle size analysis performed with ANALYSETTE 22 Nano Tec (Fritsch, Germany). The SEM appearance of RS-333 powder is presented in Figure 2.

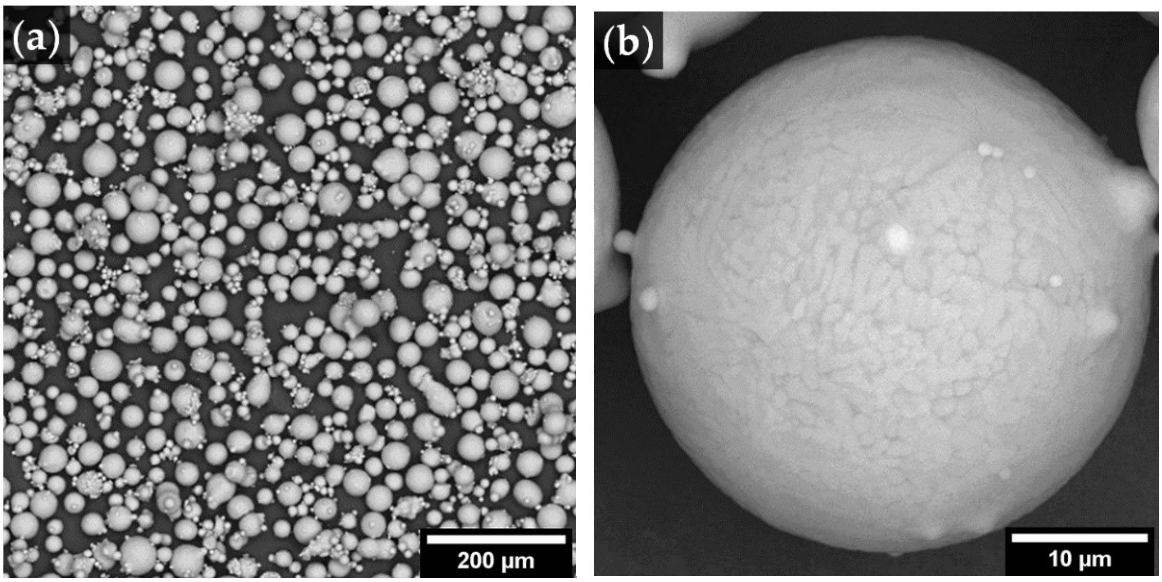

Figure 2. SEM images of RS-333 powders: (**a**) general view and (**b**) single particle microstructure.

3D printing SLM process (powder bed fusion) was carried out using EOS M290 SLM printer (Germany) equipped with 400 W Yb fiber laser unit with a wavelength of 1075 nm. Argon of high purity was used during printing in order to avoid oxidation of the powder and the melt. Scanning speed was 800 mm/s used at the laser power 370 W. Layer thickness was set to 30 μm. A post-printing heat treatment (aging) at 160 °C for 12 hours to release residual stress and to precipitate particles was applied to all printed samples. All the samples were printed using "core" parameters without special skin exposure of further surface treatment.

Preprints (www.preprints.org) | NOT PEER-REVIEWED | Posted: 12 February 2021 doi:10.20944/preprints202102.0303.v1

Flat dog bone specimens having thickness of ca. 1 mm and gauge length of 10 mm were printed in a layer-by-layer process. Sets of at least 3 samples each different orientation of main gauge axis with respect to the fast (X) and slow (Y) laser scanning directions and the growth axis (Z) as shown in Figure 3 were deliberately fabricated to study the influence of printing orientation on the mechanical response under tension. In our notation the first character corresponds to the axis aligned with gauge length, the second – to the axis aligned with gauge width. Supports used during printing were mechanically machined off to obtain samples of nominal dimensions.

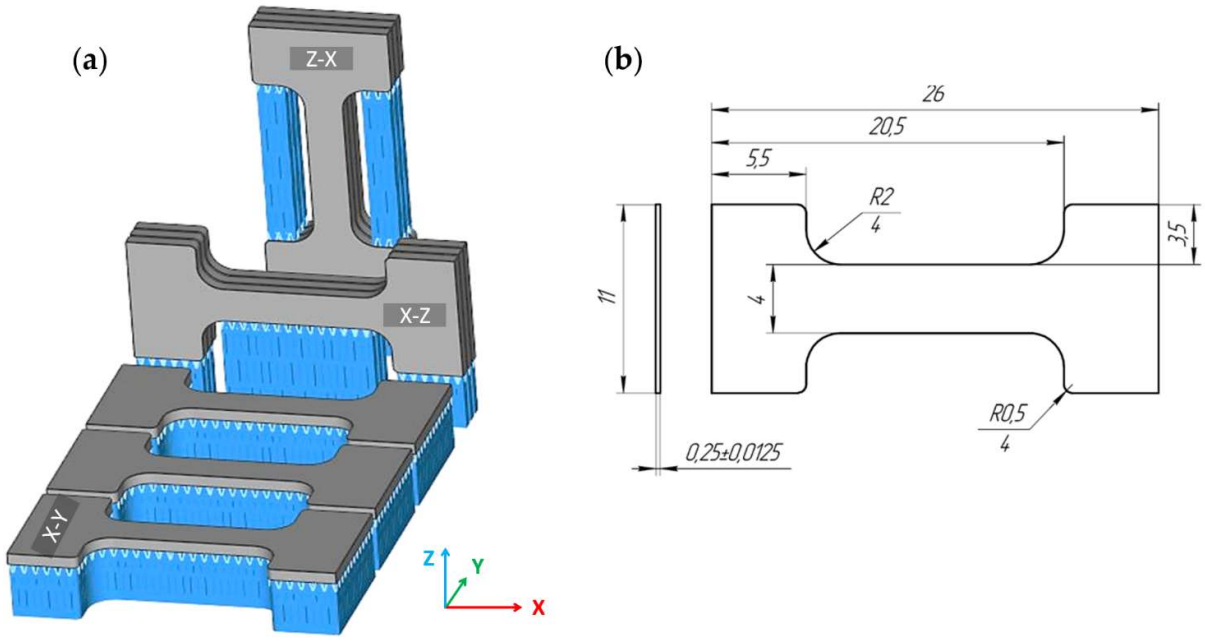

Figure 3. Test samples: (**a**) of varying orientation during printing process: X-Y, X-Z and Z-X shown from front to back, and (**b**) the nominal sample shape & dimensions.

Microstructure studies were performed after grinding and polishing using Struers laboratory equipment of as-printed sample cross-sections with no additional chemical etching. Optical microscope Zeiss Axio Observer 7 and scanning electron microscope Tescan MIRA 3 LMH (Tescan Company, Brno, Czech Republic) were applied to quantify residual pores and visualize internal fine structure respectively. As a rule, the analysis of 10 fields of cross sections in Z direction was carried out for porosity assessment.

In situ mechanical testing was facilitated with use of a Deben Microtest 1 kN testing stage placed in the chamber of Tescan Vega 3 SEM (Tescan Company, Brno, Czech Republic). The testing stage was operated under control of a Python code [18] to synchronize the mechanical loading (conducted at a permanent crosshead speed of 0.2 mm/min) with the acquisition of SEM images as exemplified in Figure 4.

Preprints (www.preprints.org) | NOT PEER-REVIEWED | Posted: 12 February 2021 doi:10.20944/preprints202102.0303.v1

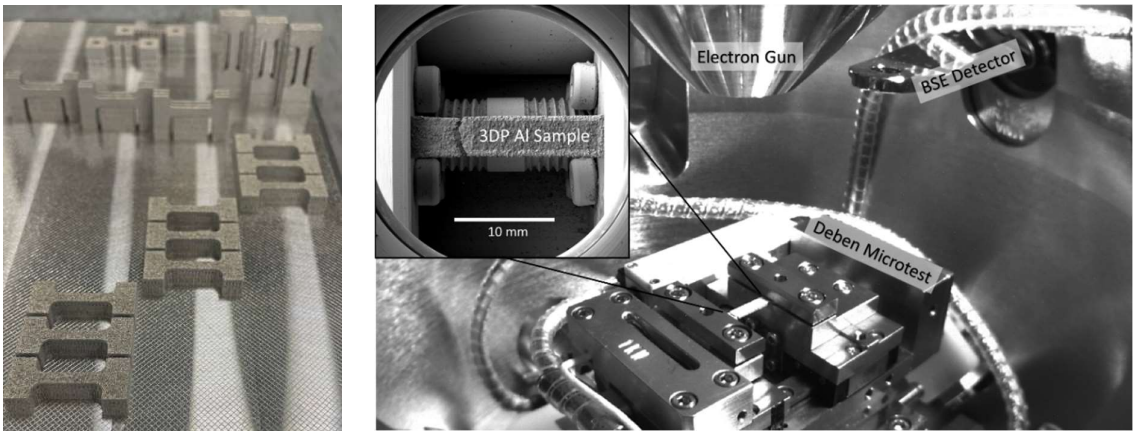

Figure 4. Appearance of 3D-printed specimens (**left**) and principal lay out of experimental set up for *in situ* SEM study of mechanical response (**right**).

SEM images were acquired at the rate of 22 s per image in the secondary electron regime using 30 kV voltage and beam spot size of 400 nm. Videos of the specimen deformation and fracture process can be found in the Supplementary Materials.

Digital image correlation analysis with the use of open-source Matlab-based software *Ncorr* [19] was applied to the series of SEM images (up to ~40-50 images depending on the data set acquired till sample break) to map the distribution of displacement and strain with subpixel resolution. The DIC algorithm compares two digital images (arrays containing digitalized intensity values) aiming to find the best match between pixel subsets. After the determination of center positions of corresponding pixel subsets, the displacement and eventually strain fields are calculated.

The definition of regions of interest and pattern quality (density of distinguishable surface features) affects both robustness and computing time in DIC analysis being performed with help of *Ncorr*. As seen in Figure 5, the pattern quality was satisfactory in terms contrast and surface feature density. In this paper 80 % of gauge area was used for DIC analysis as exemplified in Figure 6.

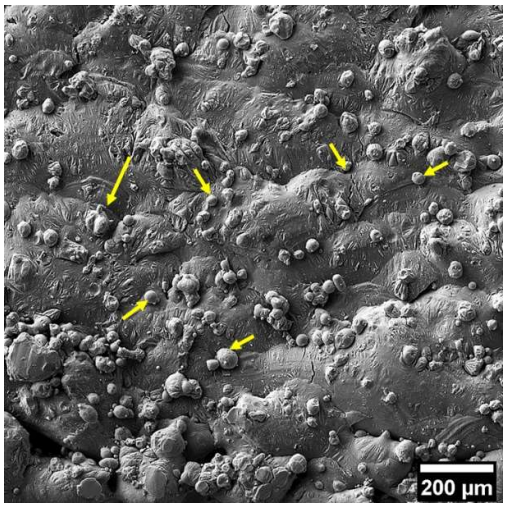

Figure 5. Appearance of surface of 3D-printed RS-333 alloy.

An important issue of elongation calibration at loading curves needs to be addressed when elastic moduli and true strains are sought to be derived from raw data acquired from a testing stage such as Deben Microtest 1kN. Crosshead displacement data is returned from Linear Variable Differential Transformer (LVDT) sensor. Despite the high accuracy of the LVDT sensor, several factors must be taken into account when loading

Preprints (www.preprints.org) | NOT PEER-REVIEWED | Posted: 12 February 2021 doi:10.20944/preprints202102.0303.v1

curves are analyzed, namely, (1) the effect of machine load frame compliance on work hardening behavior, and (2) the non-uniformity of the plastic and total strain (rate) during tensile deformation [20]. In the absence of suitable correction, the apparent deformation response of each sample depends on the nature of the test machine used. There are a few methods of so-called specimen-test machine coupling effect determination that allow detecting true deformation of the specimen during the test. The most straightforward method is the technique of total deformation. In this method the crosshead compliance correction for the displacement values of is performed using the following formulae:

$$u_{total} = u_{sample} + u_{machine}; \quad (1)$$

$$u_{sample} = u_{total} - u_{machi} \quad = u_{total} - \frac{F}{k_{machine}}, \quad (2)$$

where u_{sample} is true sample displacement [mm];

u_{total} is the displacement measured during the test, [mm];

F is the force measured during the test, [N];

$k_{machine}$ is the load frame stiffness, [N/mm], and $1/k_{machine}$ the load frame compliance [mm/N].

In this research a special "stiff" Deben calibration specimen of SS316 steel (having cross section as big 300 mm^2 and, therefore, having negligible deformation at loading) was used to plot calibration loading curve and derive $k_{machine}$ for the particular Deben Microtest 1 kN device.

On the other hand, DIC analysis is able to return strain maps in the region of interest (ROI) as well as the average strain along the main axis at the gauge length. The example of the selected ROI for each sample was similar in accordance with Figure 6. The longitudinal strain averaged over the ROI was used to plot the corresponding loading curve depicted in Figure 7 (a).

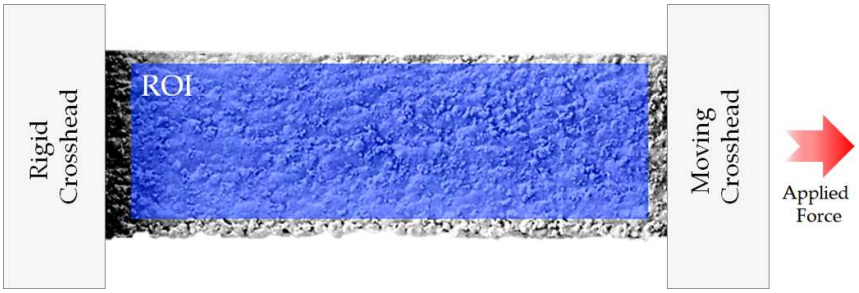

Figure 6. Illustration of typical ROI selection for grabbed SEM image.

In Figure 7 (a) the data corrected for machine compliance in comparison with DIC analysis results are illustrated for a typical sample. One can notice that DIC analysis yields reasonable values for Young's modulus for these aluminium alloys, and since so, hereinafter we consider true strains determined by means of DIC analysis.

Preprints (www.preprints.org) | NOT PEER-REVIEWED | Posted: 12 February 2021 doi:10.20944/preprints202102.0303.v1

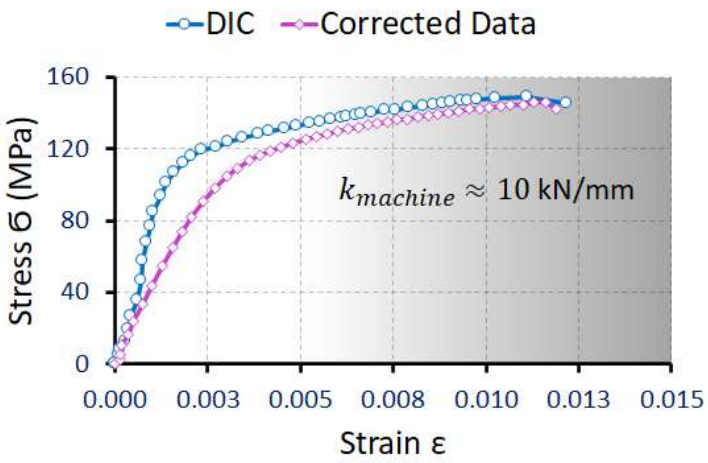

Figure 7. Processing of mechanical testing raw data: comparison of testing stage raw data with the same after crosshead compliancy correction and DIC analysis.

3. Results and Discussion

3.1. Microstructure studies

Selected parameters of powder bed fusion process applied for designed RS-333 powder result in the formation of material structure with rather low porosity and having no detectable internal hot cracks, that predetermines good service characteristics. Porosity calculated from the analysis of optical microscopy images as shown in Figure 8 is as low as 0.3% what is typical for 3D-printed aluminium alloys [21].

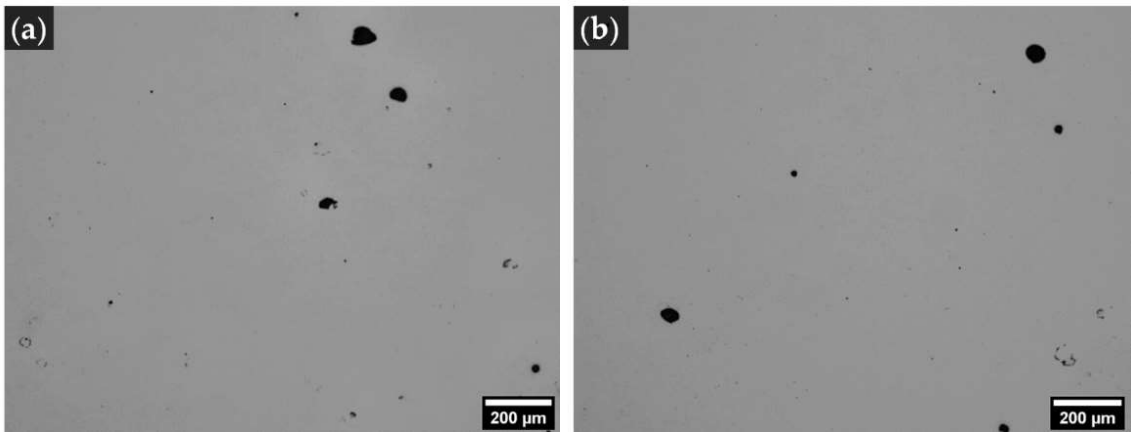

Figure 8. Representative images of porosity within SLM RS-333 aluminum alloy parts taken in the X-Z sectional plane orientation.

SEM images of structure formed in RS-333 alloy samples as a result of SLM 3D-printing and aging are represented in Figure 9. Si phase precipitates in aluminium matrix are mainly represented by the curved and dashed chains, and some smaller equiaxial particle are also noticeable suggesting that Si in RS-333 alloys is prone to some spheroidization at aging temperature applied. The improvement in heat conductivity takes place due to the decomposition of oversaturated solid solution. Aging temperature of 160 °C is, however, insufficient to complete the spheroidization eventually giving optimal combination of high heat conductivity and mechanical performance.

Preprints (www.preprints.org) | NOT PEER-REVIEWED | Posted: 12 February 2021 doi:10.20944/preprints202102.0303.v1

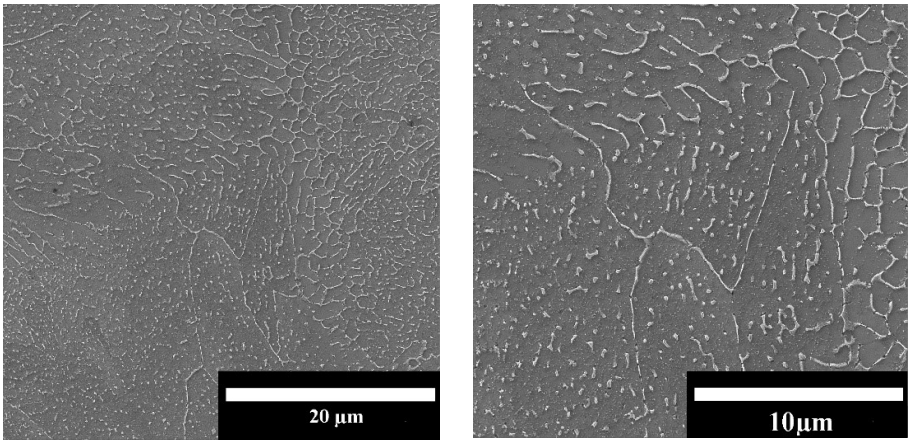

Figure 9. SEM images of RS-333 alloy microstructure following SLM printing and aging: (**a**) low and (**b**) high magnifications.

Surface appearance of a X-Z sample is represented in Figure 10 revealing relatively big (200…400 µm) and smooth clusters of molten material decorated with wrinkles and rare cracks, and inclusions of non-molten powder particles. The rests of supports are visible at the bottom edge of gauge where the clusters are apparently coarser and seem more separated with voids than in the middle zone of gauge.

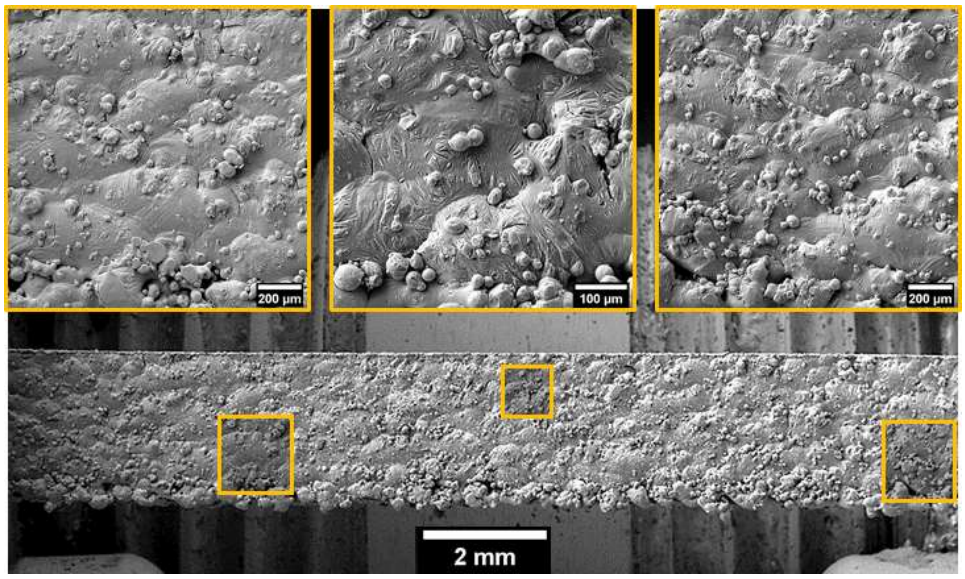

Figure 10. Surface appearance of X-Z sample with structure specification.

3.2. Mechanical performance versus sample orientation

Mechanical performance is significantly affected by the growth orientation during SLM 3D-printing as illustrated by the data represented in Figure 11 and Table 1. This technology is intrinsically complex and affecting the structure (and mechanical performance) at hierarchically scaling – from sub-micrometer up to millimeter - dimensional levels making the interpretation and sense making especially challenging in term of intensive structure characterization.

A conceptual model can be put forward to highlight the aspect of thermal history. Cooling rate from melting temperature and peak temperatures at re-heating from subsequent paths and layers in a certain material micro-volume play an important role in the structure formation including at least the following: a) solid solution composition (and Si oversaturation) after solidification; b) ultimate grain size; c) development of aging processes – volume fraction and morphology of Si precipitates.

Preprints (www.preprints.org) | NOT PEER-REVIEWED | Posted: 12 February 2021 doi:10.20944/preprints202102.0303.v1

Taking into account that the area of gauge cross-section directly depends on the sample orientation one can easily estimate characteristic times needed to print a path in plane (path time) and a layer (layer time) using the following formulae:

$$\tau_{path} = \frac{l_{path}}{v_{scan}}, \quad (3)$$

$$\tau_{lay} = \frac{S_{cs}}{d_{spot} \cdot v_{scan}}, \quad (4)$$

where τ_{path} – path time, [s]

τ_{lay} – layer time, [s];

l_{path} – path length (along fast scanning direction) in gauge zone [mm];

S_{sc} – area of cross-section in gauge zone, [mm^2];

d_{spot} – diameter of fusion zone (scaled with laser power), [mm];

v_{scan} – scanning speed, [mm/s].

Estimations in Table 1 are calculated for $d_{spot} = 300$ μm and $v_{scan} = 800$ mm/s in this research. Cooling rate for a particular micro-volume correlates with its particular position inside cross-section as well as on the geometry and area of solidified cross-section, since both temperature gradient and the area of surrounding heat sinking zone depend on latter characteristics. More accurate calculations of cooling rates can be modeled with a multi-physics FE simulation [22], but for qualitative considerations cooling rate can be taken as reverse function of path and layer time. Thus, X-Y orientation with the highest cooling rate and less frequent re-heating events ultimately brings studied alloy to the structure state corresponding to solid solution heat treatment followed by natural aging. The smallest grain size is also expected for this orientation.

In contrast, Z-X sample orientation with lowest cooling rate and frequent re-heating events tends to form the structure of annealed (with obvious recrystallization) or overaged solid solution with coarse grains. X-Z orientation occurs to be an intermediate (and, perhaps, optimal) in terms of structure (solid solution heat treatment and artificial aging) and mechanical performance.

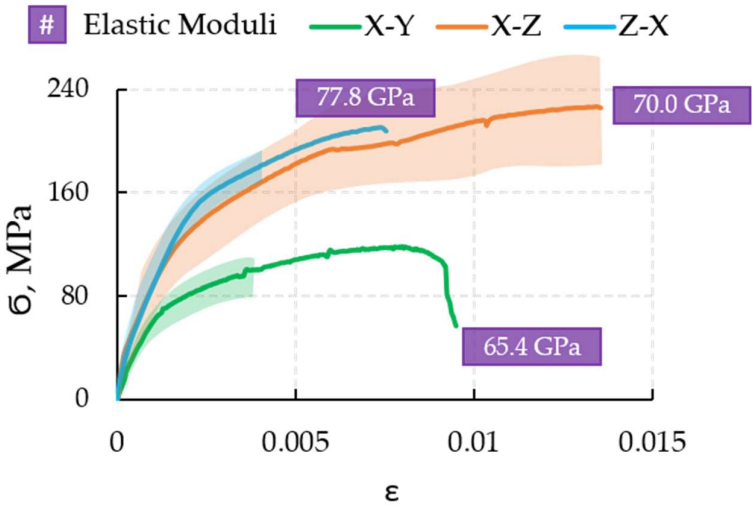

Figure 11. The typical stress-strain curves obtained for different sample printing orientations with the indication of Young's Modulus.

Table 1. Mechanical performance of RS-333 alloys samples with different sample orientation

Preprints (www.preprints.org) | NOT PEER-REVIEWED | Posted: 12 February 2021 doi:10.20944/preprints202102.0303.v1

Sample orientation	Young's Modulus, GPa	Yield Strength at 0,2 % strain, MPa	Ultimate Tensile Strength, MPa	Elongation at rupture, %	Path time, s	Layer time, s
X-Y	65.4	81	115	0.95	0,03	0,30
X-Z[1]	70.0	132	227	1.36	0,03	0,10
Z-X	77.8	150	210	0.75	0,005	0,015

[1] – sample break takes place out of gauge zone, i.e. in the rounded zone between gauge and clamp.

On the other hand, the phenomena of another nature such as generation of residual stresses, chemical inhomogeneity and dimensional unevenness are to be taken into account as factors, which may dominate over microstructure effects.

3.3 DIC insight in strain distribution

It is demonstated in Figures 12, 13 and Figure A1 that DIC analysis mapping reveals the inhomogeneous distribution of strains on the even at earliest stage of tension when a sample is macroscopically elastic. Strain distribution can be described as a wave with the wavelenght along longtidual axes of about 2 mm, that may suggest the influence of technological factors to be optimized for more strict quality control.

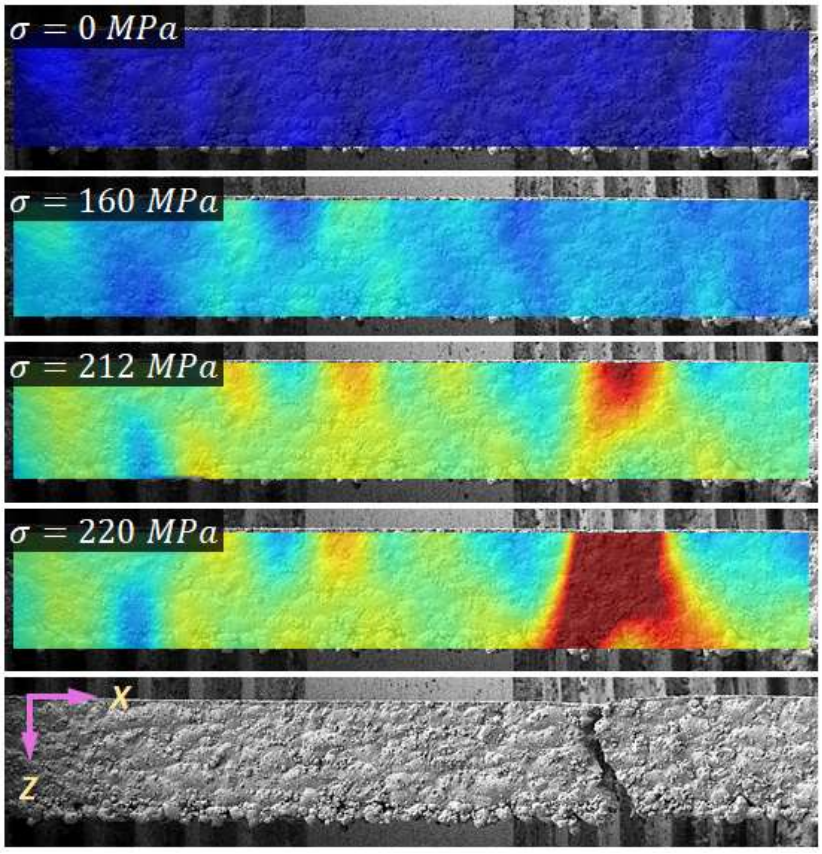

Figure 12. Demonstration of 2D DIC processing technique, namely, continuous strain localization tracking.

Localization of strain in the vicinity of future crack happens drastically and just before break that may assume the acting of rather stochastical reason such as an inhereited crack, a pore, or overgrown grain or a non-metalic inclusion. In any case, almost no necking was noticed leaving the issue of survavibility unanswered.

It is worth to note that some of samples having X-Z orienatation showed that the localization of strains and further rupture occurs in the rounded zone between gauge and clamp, where minimal layer time (and cooling rate) rapidly changes at printing. We

Preprints (www.preprints.org) | NOT PEER-REVIEWED | Posted: 12 February 2021 doi:10.20944/preprints202102.0303.v1

suppose that unevenness of cooling rates in relatively narrow space generates strong residual stresses which were not released at annealing. This gives very useful hint for good practice of SLM 3D-printing.

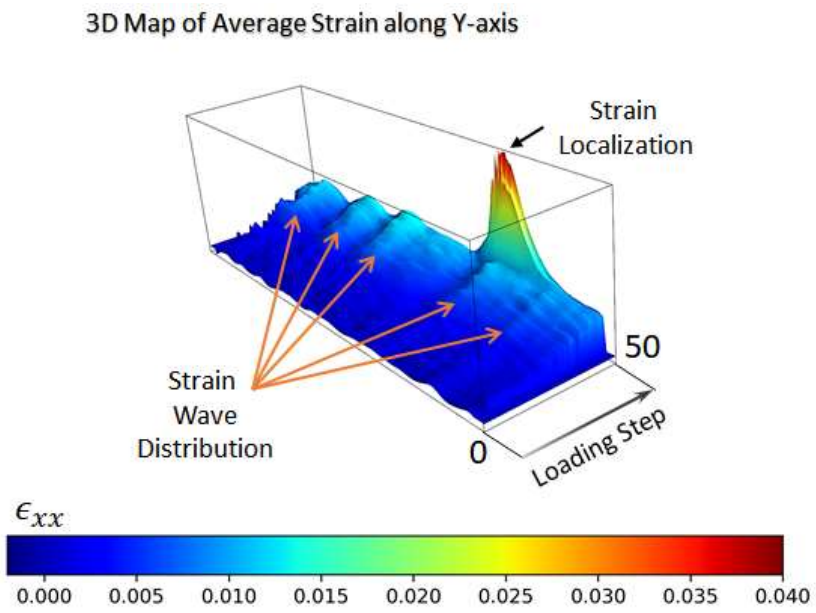

Figure 13. 3D DIC result representation with indicated strain wave-like distribution behavior.

3.4. Appearance of fracture surface

The appearance of fracture surface in Figure 14 suggests RS-333 alloy manifests some ductility during the initiation and growth of crack. The crack line occurs at an agle about 60 degree to longtidual axis, however, smaller and bigger angles were also detected.

Fracture surface (Figure 14, from left to right) has relatively smoth zone with few round pits, then zone with elongated fringle features and and finally zone with coarse pit features at the edge where the rests of support were noticed (Figure 10). It is seen for Figure 12 that the crack is initiated from flat edge zone opposite to the edge with coarse clusters and rests of supports. It seems that crack starts to grow in acordance with ductile mechanisms (smooth zone) and terminates as a brittle crack (rough zone with elongated fringle features) when substantional stress concentration is reached. The initiation of crack happens in the zone where sample growth ends and material consolidation evolves with no re-melting and re-heating. On the other hand, this zone has much more firm substrate (specimen body) than at opposite stage where only supports presents. Deeper structure investigations are required to reliably identify main physical phenomena governing the fracture behavior.

Preprints (www.preprints.org) | NOT PEER-REVIEWED | Posted: 12 February 2021 doi:10.20944/preprints202102.0303.v1

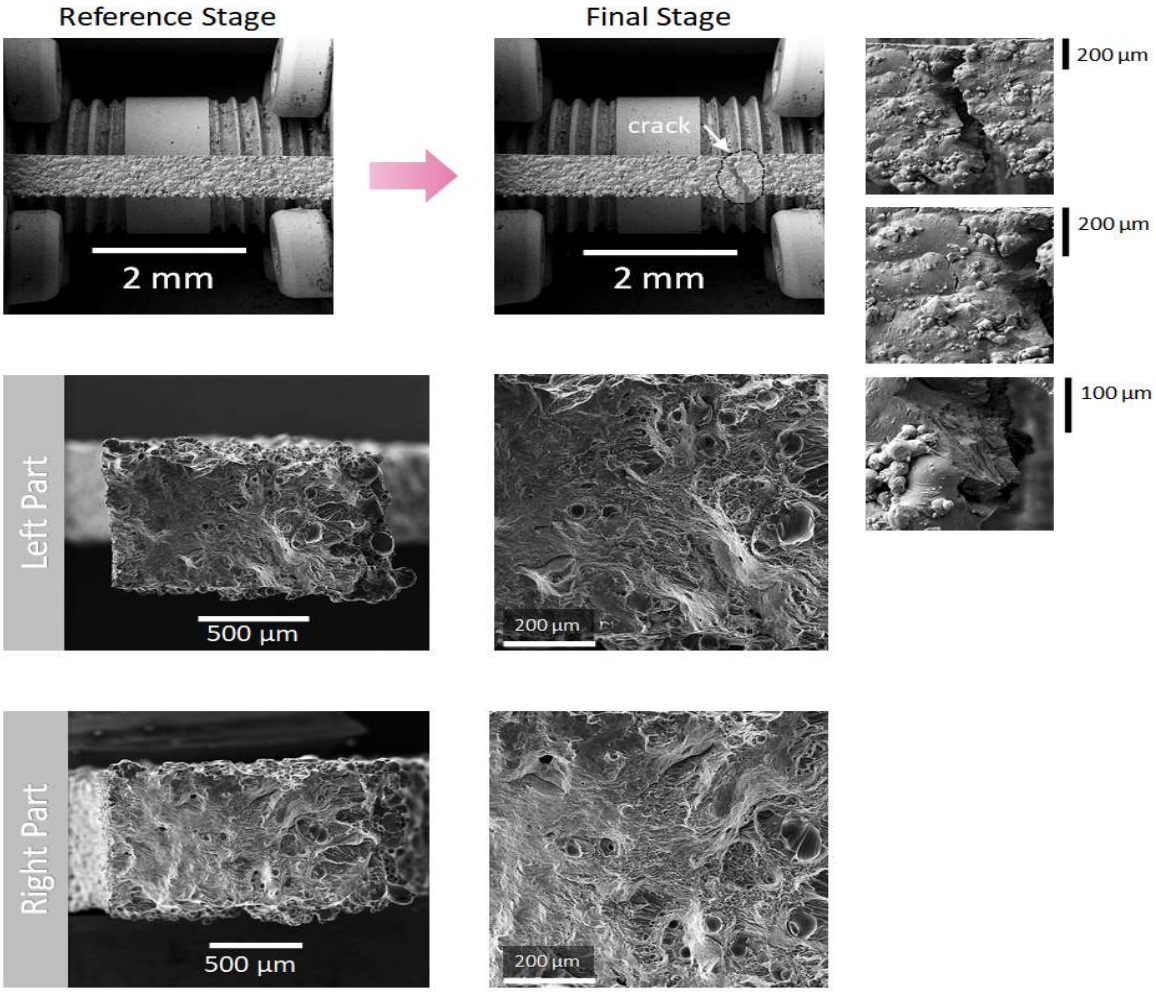

Figure 14. Appearance of fracture surface of a X-Z specimen.

4. Conclusions

For dog bone specimens SLM 3D-printed Al-Si-Mg alloy RS-333 reveals significant interrelation between the specimen orientation and mechanical tensile performance hinting a practical approach for the optimization of overall performance of heat exchanger articles. X-Z specimen orientation shows highest values of yield and ultimate strength and elongation till break at Young's modulus of about 70 GPa. *In situ* SEM studies of tension response and corresponding DIC analysis are particularly suitable to highlight peculiarities of mechanical behaviour such as unevenness of strains and their localization in the vicinity of ultimate crack. Complexity of processes (solidification at different cooling rates, frequency of re-heating events, natural and artificial aging) forming final structure requires fundamental characterization research to guide the optimization of overall performance in the most efficient way.

Supplementary Materials: Videos S1-S6: videos of specimens with different printing orientation fracture process.

Author Contributions: Conceptualization, D. and K.V.; methodology, K.V. and E.S.; software, E.S.; validation, D., A.I. and A.M.; formal analysis, E.S. and A.I.; investigation, E.S.; resources, A.I.; data curation, E.S.; writing—original draft preparation, D., E.S., A.I., and A.M.; writing—review and editing, E.S., A.I., and A.M.; visualization, E.S.; supervision, A.I. and A.M.; project administration, D.; funding acquisition, D. All authors have read and agreed to the published version of the manuscript.

Funding: This research received no external funding.

Institutional Review Board Statement: Not applicable because this study is not involving humans or animals.

Informed Consent Statement: Informed consent was obtained from all subjects involved in the study.

Data Availability Statement: The data presented in this study are available in supplementary material here.

Acknowledgments: Authors thank dear Julia Malakhova for the properly samples preparation part.

Conflicts of Interest: The authors declare no conflict of interest.

Appendix A

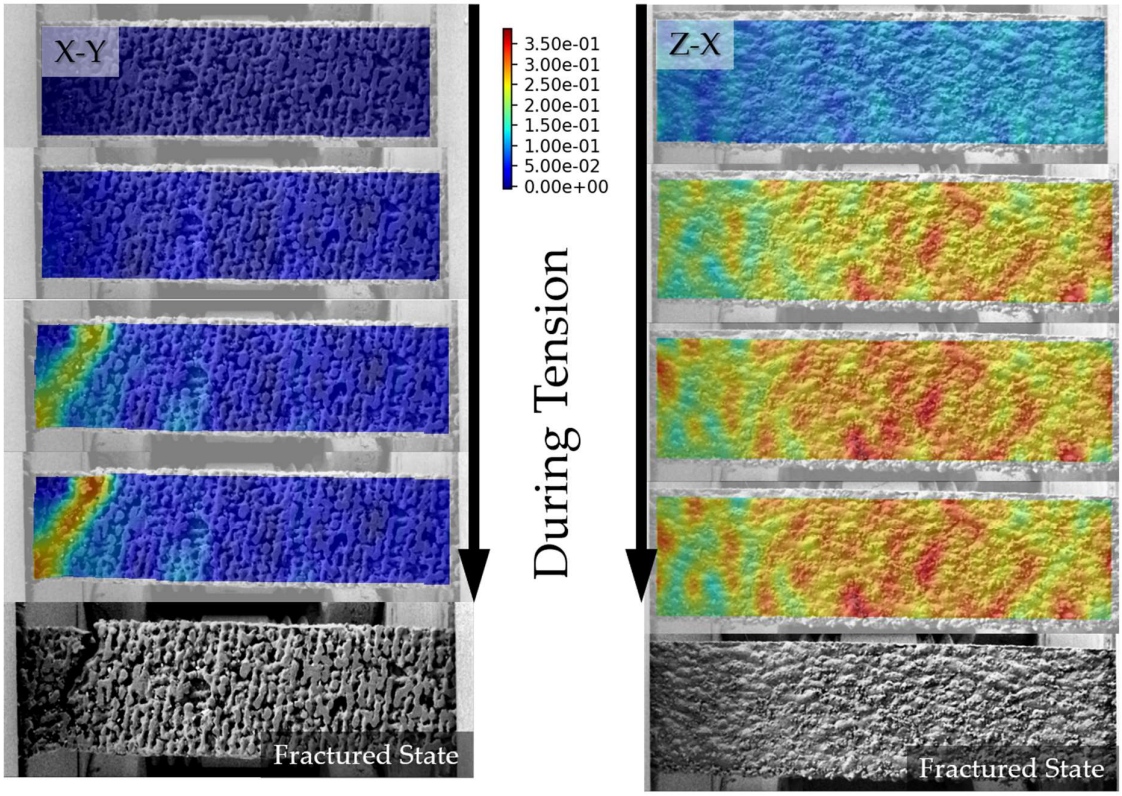

Figure A1. 2D strain distributions along loading axis for samples with different printing orientations: (**left**) X-Y and (**right**) Z-X.

References

1. Louvis, E.; Fox, P.; Sutcliffe, C.J. Selective laser melting of aluminium components / *Journal of Materials Processing Technology*, **2011**, 211(2), pp. 275–284. DOI: 10.1016/j.jmatprotec.2010.09.019
2. Thijs, L.; Kempen, K.; Kruth, J.P.; Van Humbeeck, J. Fine-structured aluminium products with controllable texture by selective laser melting of pre-alloyed AlSi10Mg powder / *Acta Materialia*, **2013**, 61(5), pp. 1809–1819. DOI: 10.1016/j.actamat.2012.11.052
3. Olakanmi, E.O.; Cochrane, R.F.; Dalgarno, K.W. A review on selective laser sintering/melting (SLS/SLM) of aluminium alloy powders: Processing, microstructure, and properties / *Progress in Materials Science*, **2015**, 74, pp. 401–477. DOI: 10.1016/j.pmatsci.2015.03.002
4. Martin, J.H.; Yahata, B.D.; Hundley, J.M.; Mayer, J.A.; Schaedler, T.A.; Pollock, T.M. 3D printing of high-strength aluminium alloys / *Nature*, **2017**, 549(7672), pp. 365–369. DOI: 10.1038/nature23894
5. Aboulkhair, N.T.; Everitt, N.M.; Ashcroft, I.; Tuck, C. Reducing porosity in AlSi10Mg parts processed by selective laser melting / *Additive Manufacturing*, **2014**, 1, pp. 77–86. DOI: 10.1016/j.addma.2014.08.001
6. Read, N.; Wang, W.; Essa, K.; Attallah, M.M. Selective laser melting of AlSi10Mg alloy: Process optimisation and mechanical properties development / *Materials and Design*, **2015**, 65, pp. 417–424. DOI: 10.1016/j.matdes.2014.09.044
7. Martin, J., Yahata, B., Hundley, J. et al. 3D printing of high-strength aluminium alloys. Nature 549, 365–369 (2017). https://doi.org/10.1038/nature23894

8. Marco Simonelli, Nesma Aboulkhair, Mircea Rasa, Mark East, Chris Tuck, Ricky Wildman, Otto Salomons, Richard Hague. Towards digital metal additive manufacturing via high-temperature drop-on-demand jetting / *Additive Manufacturing*, **2019**, 30. DOI: 10.1016/j.addma.2019.100930
9. Salimon, A.; Brechet, Y.; Ashby, M.F.; Greer, A.L. Selection of applications for a material / *Advanced Engineering Materials*, **2004**, 6(4), pp. 249–265. DOI: 10.1002/adem.200400002
10. Ashby, M.F. Materials selection in mechanical design (4th Edition) / *Butterworth-Heinemann*, **2010**, p. 640.
11. Klemens, P.G. & Williams, R.K. Thermal conductivity of metals and alloys. *International Metals Reviews* **1986**, 31(1), pp. 197–215. DOI: 10.1179/imtr.1986.31.1.197
12. Senthamarai, C.K.; *et al*. IOP Conf. Ser.: *Materials Science and Engineering* **2020**, p. 988.
13. Cebon, D.; Ashby, M.F.; Bream, C.; Lee-Shothaman, L. CES EduPack User's Manual. *Granta Design Limited*, **2009**.
14. Hanon, Muammel M., *et al.* Anisotropy Evaluation of Different Raster Directions, Spatial Orientations, and Fill Percentage of 3D Printed PETG Tensile Test Specimens. *Key Engineering Materials* **2019**, 821, pp. 167–173. DOI: 10.4028/www.scientific.net/kem.821.167
15. Sui T, Salvati E, Zhang H, *et al.* Probing the complex thermo-mechanical properties of a 3D-printed polylactide-hydroxyapatite composite using *in situ* synchrotron X-ray scattering. *J Adv Res.* **2018**, 16, pp. 113-122. DOI: 10.1016/j.jare.2018.11.002
16. E.S. Statnik, A.I. Salimon, A.M. Korsunsky. On the application of digital optical microscopy in the study of materials structure and deformation / *Materials Today: Proceedings*, **2020**, 33(4), pp. 1917-1923. DOI: 10.1016/j.matpr.2020.05.600
17. Statnik, E.S.; Dragu, C.; Besnard, C.; Lunt, A.J.G.; Salimon, A.I.; Maksimkin, A.; Korsunsky, A.M. Multi-Scale Digital Image Correlation Analysis of In Situ Deformation of Open-Cell Porous Ultra-High Molecular Weight Polyethylene Foam / *Polymers*, **2020**, 12, p. 2607. DOI: 10.3390/polym12112607
18. Statnik, E.S.; Ignatyev, S.D.; Stepashkin, A.A.; Salimon, A.I.; Chukov, D.; Kaloshkin, S.D.; Korsunsky, A.M. The Analysis of Micro-Scale Deformation and Fracture of Carbonized Elastomer-Based Composites by In Situ SEM / *Molecules*, **2021**, 26, p. 587. DOI: 10.3390/molecules26030587
19. Blaber, J.; Adair, B.; Antoniou, A. Ncorr: Open-source 2D Digital Image Correlation Matlab software / *Exp. Mech.*, **2015**, 55, pp. 1105–1122. DOI: 10.1007/s11340-015-0009-1
20. Holbrook, J.A.; Swearengen, J.C.; Rohde, R.W. Specimen-test machine coupling and its implications for plastic-deformation models / *ASTM International*, **1982**, p. 80–101. DOI: 10.1520/STP28882S
21. Nesma, T.; Aboulkhair, M.S.; Parry, L.; *et al.* 3D printing of Aluminium alloys: Additive Manufacturing of Aluminium alloys using selective laser melting. *Progress in Materials Science* **2019**, 106. DOI: 10.1016/j.pmatsci.2019.100578
22. Fernandez-Zelaia, P., Kirka, M.M., Dryepondt, S.N., Gussev, M.N. Crystallographic texture control in electron beam additive manufacturing via conductive manipulation. *Materials and Design* **2020**, 195. DOI: 10.1016/j.matdes.2020.109010